Journal of Computational Design and Engineering, 2022, 9(2), 279–295

https://doi.org/10.1093/jcde/qwab004
Journal homepage: www.jcde.org

RESEARCH ARTICLE

Application of artificial neural network for lubrication performance evaluation of rough elliptic bore journal bearing

Sushanta Kumar Pradhan, Prabhudatta Mishra and Prakash Chandra Mishra *

Department of Mechanical Engineering, Veer Surendra Sai University of Technology, Burla 768018, Odisha, India

*Corresponding author. Email: prabasmishra73@gmail.com http://orcid.org/0000-0001-9576-0026

Abstract

In this study, rough elliptic bore journal bearing performance is predicted using an artificial neural network (ANN) technique. The effects of non-circularity and roughness are quantified to elliptic and isotropic in macro and micro scale, respectively. The numerically estimated performance parameters like load, friction, and flow-in at different eccentricities [0.3 (low), 0.5 (medium), and 0.8 (high)], non-circularities [0.5 (low), 1.0 (medium), and 2.0 (high)], and roughness factors [0.1 (low), 0.2 (medium), 0.3 (medium), and 0.4 (high)] are used to train and build the ANN model. The training continued until the maximum mean square error is achieved, and the best-fitting plot is generated. With a confidence level of 99.75% or an *R*-value of 0.99757, the results predicted are found to be satisfactory.

Keywords: artificial neural networks; isotropic; journal bearing; Levenberg–Marquardt; load; friction; flow-in

Abbreviation

ANN:	Artificial neural network
ICA:	Imperialism competitor algorithm
LCC:	Load-carrying capacity
MSE:	Mean squared error
Nu:	Nusselt number
PSO:	Particle swarm optimization
R^2:	Determination coefficient
TBD:	Tunnel boring machine
TiO_2:	Titanium dioxide
ZnO:	Zinc oxide

Nomenclature

c :	Radial clearance (mm)
e :	Eccentricity (mm)
G :	Non-circularity
h :	Film thickness (μm)
H :	Non-dimensional film thickness
r_j :	Radius of journal (mm)
R_{min} :	Major radius (mm)
R_{maj} :	Minor radius (mm)
U :	Entraining velocity (m/s)
W^* :	Non-dimensional load

Received: 24 November 2020; **Revised:** 11 January 2021; **Accepted:** 14 January 2021

x, y :	Coordinate axis
Y :	Roughness parameter
Z :	Axial direction
θ :	Film position from load line
α :	Load angle
ϕ :	Attitude angle
β :	Length-to-diameter ratio
η :	Coefficient of viscosity
ε :	Eccentricity ratio
$or f$:	Overrelaxation factor
Π :	Film thickness function
ζ :	Expectancy operator
F :	Non-dimensional friction
Q :	Non-dimensional flow-in
ω :	Angular velocity
u_{av} :	Average entraining velocity
L :	Length of journal
N :	Number of date points

1. Introduction

Journal bearing is a full fluid film bearing. It is also known as bearing of infinite life. Metal-to-metal contact between the rotating journal and the stationery bore is entirely absent due to the thick lubricant film (5–100 μm) in the clearance space. Such bearings have broad applications in industries to support vital components like gas turbines, crankshaft, connecting rods, etc. The tribological performance parameters such as load-carrying capacity (LCC; Sivák *et al.*, 1981), friction force, flow-in, and side leakage were investigated from smooth circular journal bearing in static and dynamic conditions in many works reported in literature. The presence of ellipticity in bore (Crosby, 1992) has significant effects on journal bearing performance. It is observed in various studies (Christensen, 1969; Christensen & Tonder, 1973; Mishra, 2013) that bore ellipticities up to 3.0 bring better stability for journal bearing. Again, microscopic irregularities like surface roughness have positive effects on bearing performance (Binu *et al.*, 2014; Liang *et al.*, 2014; Li *et al.*, 2019). Bearing surface roughness with parameters up to 10% of roughness height has better impact on LCC (Christensen, 1969; Christensen & Tonder, 1973). A transverse pattern of roughness has a better LCC, while the longitudinal pattern has more side leakage (Christensen, 1969). Further, isotropic roughness orientation has a good compromise between LCC and side leakage. Roughness in a bearing bore is quantified using stochastic (Christensen, 1969) and deterministic models. Through stochastic method, the probabilistic density distribution of roughness height is plotted and compared with Gaussian distribution (Christensen, 1969; Christensen & Tonder, 1973), while in deterministic model, the roughness influence on operating characteristics is emphasized. In both cases, the nature of impact depends on the orientation of the roughness (transverse, longitudinal, and isotropic).

Metal nanoparticles like TiO_2, ZnO, and $ZnAl_2O_4$ improve the lubrication properties. The addition of such nanoparticle additive (Shahnazar *et al.*, 2016; Laad & Jatti, 2018) enhances the LCC of journal bearing (Binu *et al.*, 2014). The LCC can also be enhanced due to the use of multilobe as the bearing sleeve constraint improves the LCC (Li *et al.*, 2019). Stability (Pai *et al.*, 2012; Mishra, 2013) of journal bearing depends on spring constant and damping coefficient. These parameters are used to find the critical mass and the whirl ratio. The highly non-linear whirl and whip of the bearing are due to the combined effect of shaft misalignment, bore ellipticity, and roughness orientation. In the journal bearing analysis, minimal works are reported in finite element simulation (Shen *et al.*, 2012). Shen *et al.* (2012) used a thermal wear simulation program in ABACUS to analyse the dynamic wear process of bearing. There are very limited number of works reported on the experimental aspect of journal bearing, because of the requirement of interfacing and the associated problems of data acquisition system with moving shaft and micro size conjunctional dimension.

So many parameters of a journal bearing while in operation and their interdependence often make it a complicated system to understand the correct combination of parameters for optimum performance. Artificial neural network (ANN) is considered to be one of the advanced tools to train data from simulations or experiments of journal bearing operation. The ANN found its application in estimating the wear using Response surface methodology (RSM) and LMBP [Levenberg–Marquardt (L–M) back-propagation] neural network architecture (Kannaiyan *et al.*, 2019). Hayajneh *et al.* (2009) used ANN to predict the quantity of material loss due to the Al–Cu–Si carbide wear. They studied the effect of Cu as an alloying element and Si carbide as reinforcement particle to Al-4 wt % Mg metal matrix. The results were compared with the experiment and relative errors were found to be 2.4% of the non-coded values. There are a number of ANN applications found in wear estimation (Zhang *et al.*, 2002; Genel *et al.*, 2003; Rashed & Mahmoud, 2009; Xiao & Zhu, 2010; Leema *et al.*, 2015). Even applying the ANN, the optimization of emission characteristics was carried out for different injection timings and engine load at different blend mixtures. This ANN application revealed that blended fuels provide better engine performance and improved emission characteristics (Sharma *et al.*, 2015). Bhowmik *et al.* (2017) developed an ANN model to study the synthesis of $MnFe_2O_4$ and Mn_3O_4 magnetic nano-composites for enhanced properties of adsorption. Through this model, they predicted Cr (VI) ion removal with a minimum mean squared error (MSE) of 15.4 × 104 and a maximum R^2 of 0.98. Similar work of ANN on adsorption of mixed-phase $CaFe_2O_4$ magnetic nano-composites (Bhowmik *et al.*, 2019) predicted the second-order kinetic and Langmuir isotherm to best fit with experimental data. The maximum MO dye absorption capacity in this case is found to be of 344.83 mg/.

Application of ANN to study the chemical route synthesis of nanoparticles (Debnath *et al.*, 2015), to study the kinetic and equilibrium isotherm (Debnath *et al.*, 2015), and to study the efficiency of toxic Congo Red dye adsorption from aqueous solution (Deb *et al.*, 2017) was found reasonable. The ANN application in rock mechanics and blasting phenomena is also reported. Armaghani *et al.* (2017) developed a hybrid intelligence model to predict the TBD penetration rate in hard rock conditions. In this case, the intelligence was created using 1286 data sets with combined particle swarm optimization (PSO), ANN, and imperialism competitor algorithm (ICA). Such a hybrid model was found to yield a better result than simple ANN. Using this hybrid technique, the air-over pressure (Armaghani *et al.*, 2015) in air blast was successfully predicted. Also, the maximum bearing capacity of rock socketed piles was accurately predicted using this algorithm (Armaghani *et al.*, 2015). Parrales *et al.* (2019) applied the ANN to find Nusselt (Nu) number correlations in heat transfer analysis of helical double pipe evaporator. With a coefficient of determination, $R^2 > 0.99$ and one node in the hidden layer, this model used Prandtl and Jacob liquid as input variables. Using ANN, the Nu for biphasic flow with an accuracy of ±0.2 for annular Nu and ±4 for the inner Nu was successfully evaluated.

Based on this broad literature survey, it is observed that a significant number of research works reported on bearing

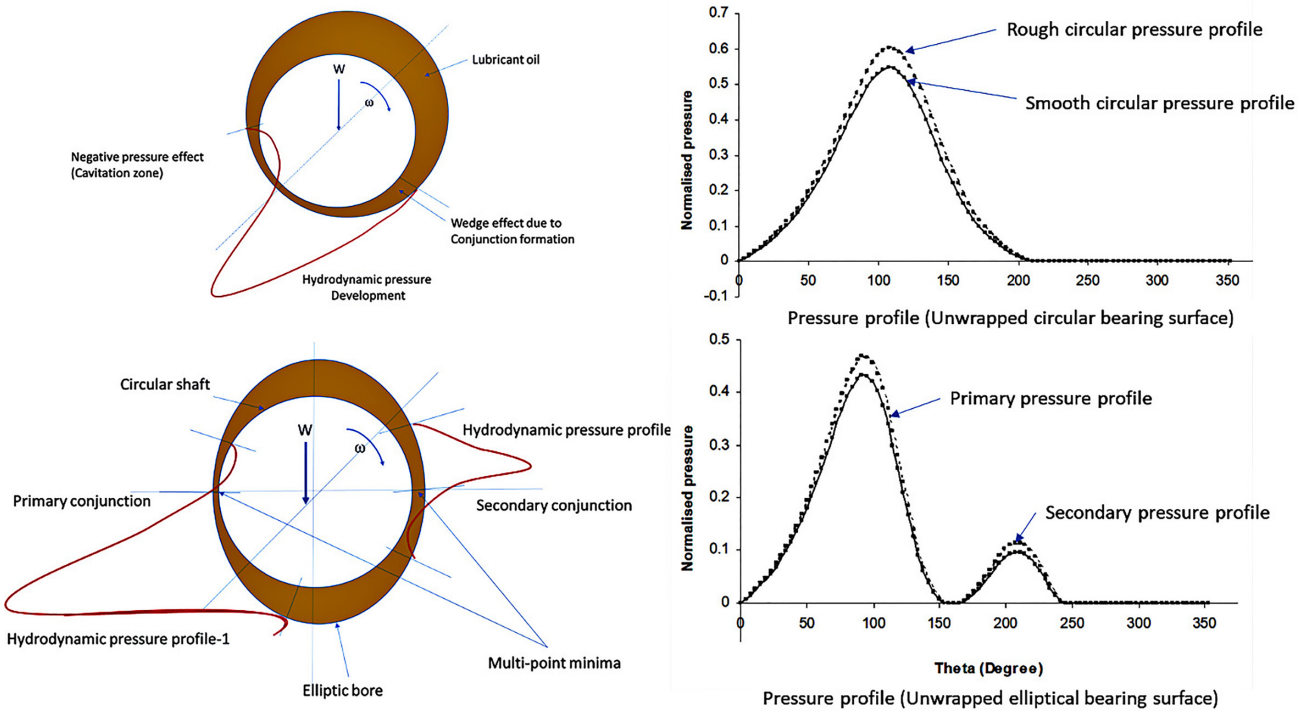

Figure 1: Mechanism of hydrodynamic pressure lubrication in circular and elliptic bore journal bearing.

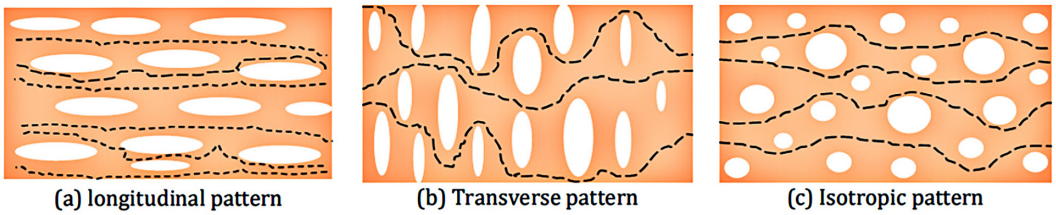

Figure 2: Roughness pattern of bearing surface.

performance analysis, while ANN applications were found in the area of wear analysis, manufacturing, material processing, chemical synthesis, rock mechanics, etc. Its application to journal bearing in general and rough elliptic bearing in particular was never reported, which is the objective of this research work.

2. Material and Methods

2.1. Configuration of rough elliptic bore journal bearing

Journal bearing bore is manufactured through machining operation like boring or turning. Due to machine tool vibration, the non-circular geometry of the bore is bound to occur in the inner surface. Crosby (1992) quantified these irregularities as oval or elliptical, which is given in equation (1).

$$G = \frac{\delta - 1}{\psi} \tag{1}$$

Here, 'G' is the non-circularity/ellipticity coefficient, 'δ' is the ratio of major radius to the minor radius (R_{maj}/R_{min}). If the value of $G = 0$, then $\delta = 1$ leads to the bore to be circular. The maximum value of G ever taken in the analysis is 3 (Mishra, 2013), which has good stability. In this analysis, we consider G, δ, and ψ as ellipticity parameters, which are interdependent. Figure 3a–d shows the charts of ψ versus G, δ versus G, δ versus ψ, and Δ versus ψ. The value of G increases with an increase in the value of δ and ψ.

Figure 1 shows the mechanism of hydrodynamic lubrication in the case of circular and elliptic bore bearing. Due to the formation of a double wedge shape (lubrication conjunction), two different pressure bumps appeared. The pressure profile on the unwrapped bearing surface shows more pressure development due to isotropic roughness in the bearing surface. Figure 2 shows the different pattern of roughness, which is expected in the bearing surface.

Like ellipticity, roughness is also bound to occur in a bore surface, as the small amplitude vibration of the tool during manufacturing is replicated on a machined surface (Christensen & Tonder, 1973). The orientations are classified to be transverse, longitudinal, or isotropic as pointed out in Fig. 2. Christensen and Tonder (Christensen, 1969) considered the roughness as an extra component in the film thickness, which is known to be stochastic. It is given in equation (2).

$$h_s = \begin{vmatrix} h_s(\theta, z, \xi) & \text{(Isotropic)} \\ h_s(z, \xi) & \text{(Longitudinal)} \\ h_s(\theta, \xi) & \text{(Transverse)} \end{vmatrix} \tag{2}$$

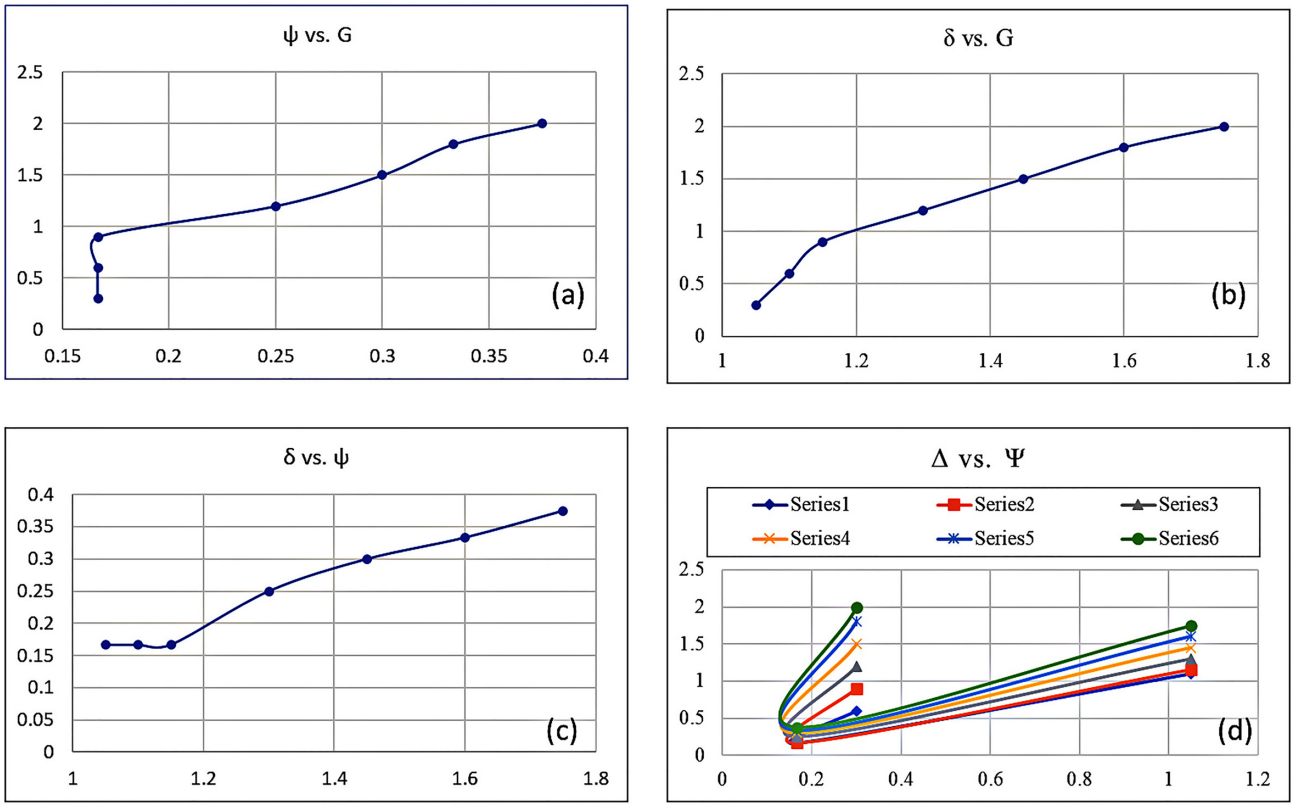

Figure 3: Ellipticity parameters inter-dependence.

Hence, the film thickness for rough elliptic bore journal bearing is upgraded as follows:

$$h = c + G\cos^2(\theta - \alpha) + e\cos(\theta - \phi) + h_s(\theta, z, \xi). \quad (3)$$

Hence, the non-dimensional film thickness is as follows:

$$H = 1 + G\cos^2(\theta - \alpha) + \epsilon\cos(\theta - \phi) + H_s(\theta, z, \xi). \quad (4)$$

2.2. Numerical method for rough elliptic bore lubrication performance

The Reynolds equation for this rough elliptic case as per Christensen and Tonder (1973) is taken as

$$\frac{\partial}{\partial x}\left(\frac{\partial P}{\partial x}\zeta_1(H)\right) + \frac{\partial}{\partial z}\left(\frac{\partial P}{\partial z}\zeta_2(H)\right) = 6\eta u\frac{\partial}{\partial x}\zeta_3(H). \quad (5)$$

For an elliptic bore with isotropic roughness (Christensen, 1969), the equation modified to

$$\frac{\partial}{\partial x}\left(\frac{\partial P}{\partial x}E(H^3)\right) + \frac{\partial}{\partial z}\left(\frac{\partial P}{\partial z}E(H^3)\right) = 6\eta u\frac{\partial}{\partial x}E(H). \quad (6)$$

Here, $E(H^3)$ are expectancy operators, which can be evaluated as

$$E(H^3) = \int_{-c}^{c} H^3 f(h_s)\,dh_s = \int_{-c}^{c} (h + h_s)^3 f(h_s)\,dh_s = h^3 + 3h\sigma^2. \quad (7)$$

Here, 2c is the maximum peak to peak roughness distance, and σ^2 is the variance of the height variation.

$$\sigma^2 = \int_{-c}^{c} h_s^2 f(h_s)\,dh_s = \frac{c^2}{9} \quad (8)$$

The different expectancy operators for isotropic surface and their corresponding value in terms of G, H, and Y are given in Table 1.

Equation (6) is discretized using the central finite difference method. A numerical technique is adopted to solve the discretized equations for hydrodynamic pressure through effective influence Newton–Raphson method. To speed up the iterative process, the overrelaxation factor in the case of oil-lubricated bearing is introduced as follows:

$$P_{i,j}^{K} = P_{i,j}^{K} + orf\left(P_{i,j}^{K+1} - P_{i,j}^{K}\right). \quad (9)$$

The convergence criteria for pressure error are set as per equation (10).

$$\text{Error} = \sum_{i}^{n}\sum_{j}^{m}\left|P_{i,j}^{K+1} - P_{i,j}^{K}\right| \le 0.005 \quad (10)$$

The error tolerance ≤0.0015 has been decided by trials. The convergence criteria are decreased gradually like 0.1, 0.01, 0.001, and 0.0001, and the result is compared for successively fell convergence (Mishra, 2013). If the result shows very little change between two sets of convergence, the higher value of $P_{i,j}$ is considered.

In the beginning, the pressure at all nodes is taken as zero. This automatically satisfies the boundary conditions on the left, top, and bottom sides, i.e. at $\theta = 0$, $Z = 0$, and 1 (Mishra, 2013). The value of $P_{i,j}$ is found by starting with $P_{1,1}$ and either moving zigzag to the right-hand corner node within the boundary or by moving vertically and zigzag to the corner to satisfy the boundary conditions. The $P_{i,j}$ is never allowed to become negative by setting any negative value to zero (Mishra, 2013). Once the error

Table 1: Expectancy operator values.

Film terms	Value	Expectancy function
$E(H)$	$1+G\cos^2\theta+\epsilon\cos\theta$	$\zeta_3(H)$
$E(\frac{1}{H})$	$\frac{35}{37Y^7}\{6(Y^2-H^2)\log(\frac{Y+H}{Y-H})+\frac{2}{5}YH(15H^4-40Y^2H^2+33Y^4)\}$	$\zeta_4(H)$
$E(H^3)$	$H^3+\frac{HY^2}{3}$	$\zeta_1(H)$,$\zeta_2(H)$

Table 2: Non-dimensional to dimensional correlation of parameters.

Description	Non-dimensional to dimensional relations
Hydrodynamic pressure	$p^*=\frac{pc^2}{\eta\omega^2r_j{}^2L}$
Load	$W^*=\frac{Wc}{\eta\omega r_j{}^2L}$
Friction	$F^*=\frac{Fc}{\eta\omega r_j{}^2L}$
Flow-in	$Q_{in}^*=\frac{Q_{in}}{u_{av}Lc}$

of convergence is reached between two consecutive iterations as per equation (10), the process of iteration is stopped.

The LCC of the bearing is given as follows:

$$W_x=\sum_0^{2\pi}\sum_0^1(P\sin\theta)\Delta\theta\Delta Z, \tag{11}$$

and

$$W_z=\sum_0^{2\pi}\sum_0^1(P\cos\theta)\Delta\theta\Delta Z. \tag{12}$$

Hence,

$$W=\sqrt{W_x^2+W_z^2}$$
$$\phi=\tan^{-1}\left(\frac{W_z}{W_x}\right). \tag{13}$$

Here, ϕ is the load angle. The friction force is the integration of shear over the grid area. The shear stresses at the pressure zone and cavitation zone are different (Christensen & Tonder, 1973). The friction force considering these issues is given in equation (14).

$$F=\underbrace{\sum_0^{\pi}\sum_0^1\left[\frac{1}{2}\frac{\partial P}{\partial\theta}\zeta_3(H)+\eta u(\zeta_4(H)-\zeta_5(H))\right]}_{\text{Pressure Zone}}+\underbrace{\sum_{\pi}^{2\pi}\sum_0^1[\eta u(\zeta_4(H)-\zeta_5(H))]}_{\text{Cavitation Zone}} \tag{14}$$

The mean oil flows per unit width along the direction of rotation and direction of side leakage are, respectively, given as

$$q_\theta=\frac{u}{2}\zeta_3(H)-\frac{1}{12\eta}\frac{\partial P}{\partial x}\zeta_1(H) \tag{15}$$
$$q_Z=-\frac{1}{12\eta}\frac{\partial P}{\partial Z}\zeta_2(H). \tag{16}$$

The total flow-in and side leakages are obtained by integrating equations (15) and (16), respectively.

The non-dimensional parameters discussed in the model are presented Table 2, with their dimensional relationships. In the non-dimensional pressure, load, and friction, the effect of viscosity is present.

2.3. ANN for rough elliptic bore lubrication

2.3.1. *ANN model*

ANN is an advanced simulation and modelling tool that uses computational skills integrated into the human brain. It performs learning and prediction in a sequence to study various scientific data and suggests favourable combinations. The ANN deals with some artificial neurons, organized in a definite structure and interacting with each other with the help of weight (Bhowmik *et al.*, 2019). Since last few years, the ANN has found its application in various fields of science and technology such as manufacturing, robotics, metal processing, etc. The current ANN method is developed using the neural network toolbox of the MATLAB software. In order to observe the performance, the number of neurons is varied from 1 to 20 in the hidden layers. Further, the value of mean square error (MSE) and

Table 3: Statistical details of model input/output parameters.

Symbol	Unit	Category	Min^m	Max^m	Mean
G	Non-dimensional	Input	0	2.0	1.0
Y	Non-dimensional	Input	0	0.3	0.1
ε	Non-dimensional	Input	0.1	0.9	0.45
β	Non-dimensional	Input	0.5	2.0	1.0
W_{is}	Non-dimensional	Output	3.8245	24.5895	9.6155
W_{th}	Non-dimensional	Output	1.302	6.3785	3.8013
F_{is}	Non-dimensional	Output	16.7014	102.67	47.3882
F_{th}	Non-dimensional	Output	5.3692	58.46	24.675
Q_{is}	Non-dimensional	Output	4.4388	6.4226	5.4006
Q_{th}	Non-dimensional	Output	5.2415	7.0872	6.0289

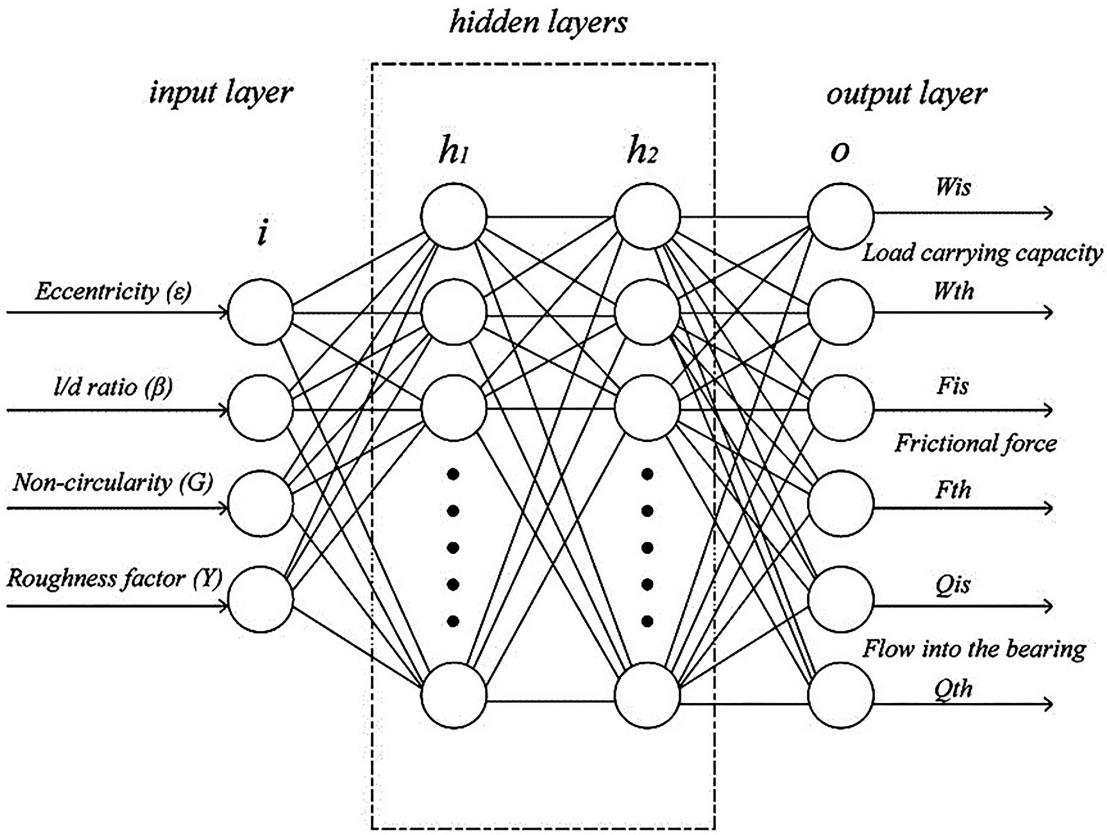

Figure 4: Architecture of neural network model.

determination coefficient (R^2) of training and testing of the data set were studied for analysing the performance.

The equations for MSE and R^2 are, respectively, given by

$$\mathrm{MSE} = \frac{1}{N}\sum_{i=1}^{N}\left(\left|y_{\mathrm{prd,i}} - y_{\mathrm{exp,i}}\right|\right)^2 \tag{17}$$

$$R^2 = 1 - \frac{1}{N}\frac{\sum_{i=1}^{N}\left(y_{\mathrm{prd,i}} - y_{\mathrm{exp,i}}\right)}{\sum_{i=1}^{N}\left(y_{\mathrm{prd,i}} - y_m\right)}. \tag{18}$$

Here, $y_{\mathrm{prd,i}}$ is the model predicted value, $y_{\mathrm{exp,i}}$ is the experimental value, and y_m is the arithmetic mean of all experimental data. N is the number of data points. There are 162 data points considered for the model, out of which 70% of total data points (114) were considered for training, 15% (24) for testing, and 15% (24) for validation. The input parameters are chosen as G, Y, ε, and β. The raw data (both input and output) are normalized (0–1) using equation (19). The statistical details of input/output parameters are given in Table 3.

$$X_{\mathrm{norm}} = \frac{X - X_{\mathrm{min}}}{X_{\mathrm{max}} - X_{\mathrm{min}}} \tag{19}$$

ANN model of the finite journal bearing was constructed using four and six parameters in the input and output layers, respectively. The performance parameters, i.e. LCC, friction, and flow of the lubricant into the bearing, were considered as targets and the non-circularity (G), L/D ratios(β), roughness parameters (Y), and eccentricities (ε) were used as the input parameters. Figure 4 shows the architecture of the neural network model. Here, the data were used to train and build the ANN model and obtain the trained results. The ANN model training was conducted for several cycles until the minimum mean square error (MSE) was reached, and best-fitting plots were obtained to stop the training. These outputs are compared to the targets, and the error data were calculated and discussed. Various plots and performance graphs were also obtained using the ANN tool and discussed in the result analysis section.

Table 4: Comparison of the number of neurons (1–20) in the hidden layer.

No. of neurons	MSE	R^2	No. of neurons	MSE	R^2
1	0.03239	0.7641	11	0.00262	0.9821
2	0.01863	0.8583	12	0.00274	0.9638
3	0.01653	0.9035	13	0.00338	0.9853
4	0.01487	0.9346	14	0.00448	0.9763
5	0.00698	0.9487	15	0.00568	0.9608
6	0.00387	0.9884	16	0.00638	0.9370
7	0.00208	0.9832	17	0.00946	0.9196
8	0.0178	0.9794	18	0.00997	0.9143
9	0.00154	0.9747	19	0.01458	0.9096
10	0.00146	0.9854	20	0.01856	0.8983

A comparison of the number of neurons in the hidden layer is given in Table 4. Based on the maximum value of R^2 and the minimum value of MSE, the optimal network's topology is configured. The most challenging task to be accomplished in ANN modelling is to determine the best network architecture in terms of selecting both the proper ANN training algorithm and the number of hidden nodes in hidden layers. Armaghani *et al.* (2016,

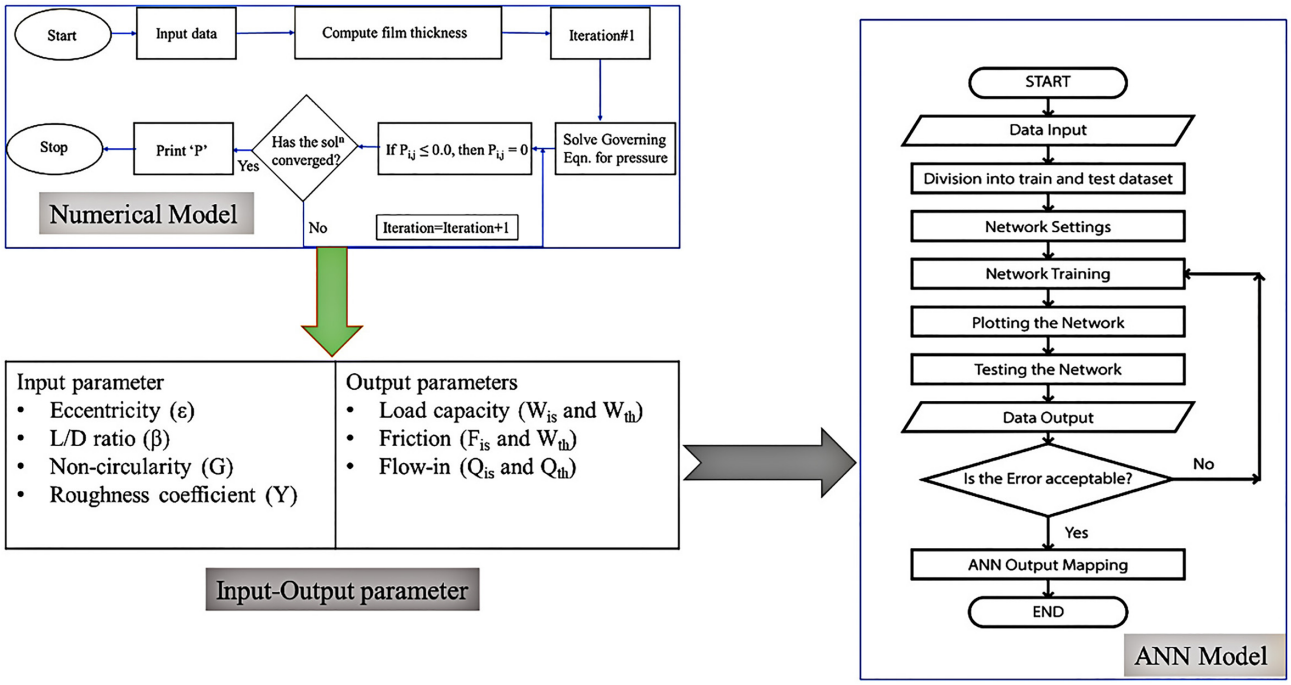

Figure 5: Flow chart for combined numerical and ANN model.

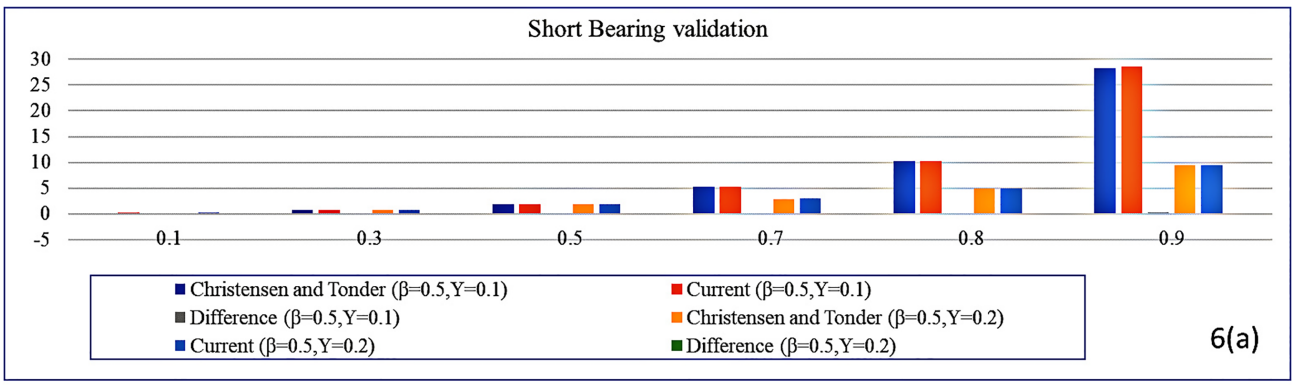

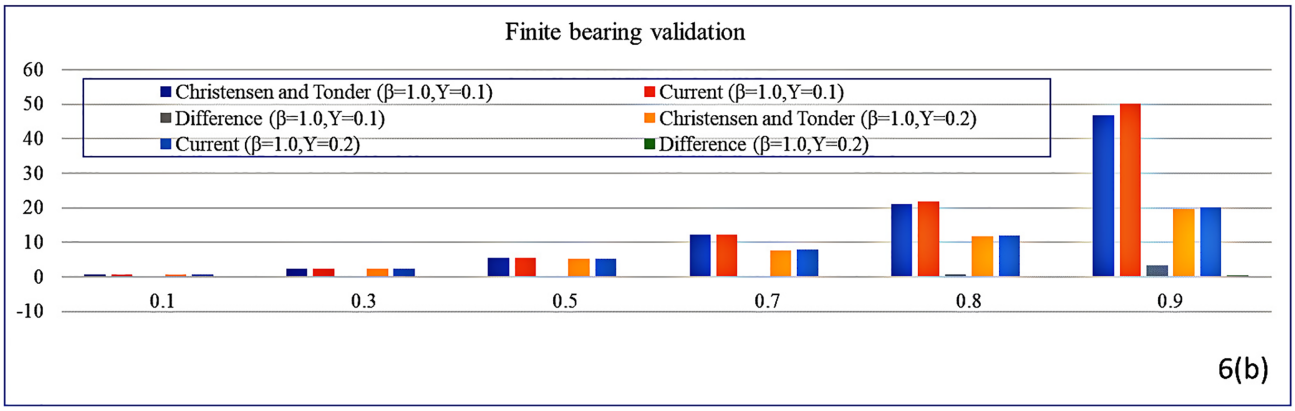

Figure 6: Validation of the numerical model.

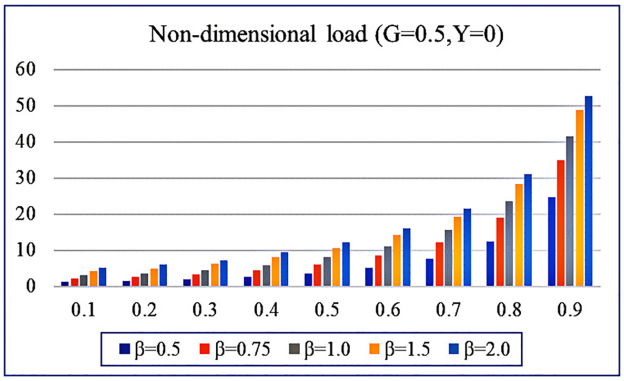

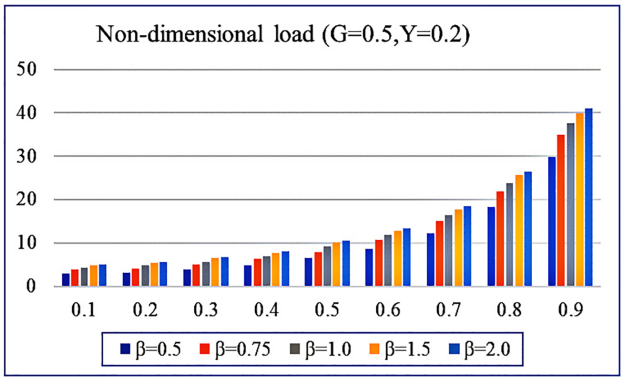

Figure 7: Load response to eccentricity for smooth and rough elliptic bore Case I.

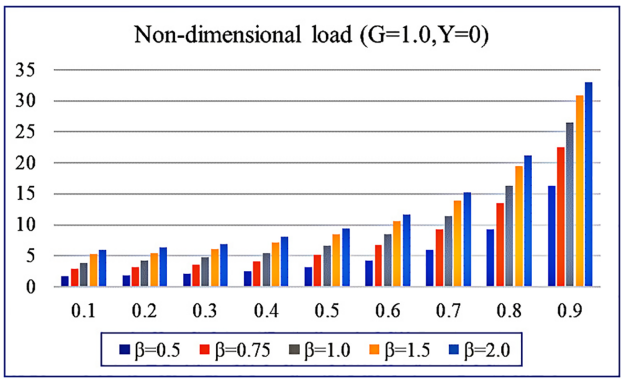

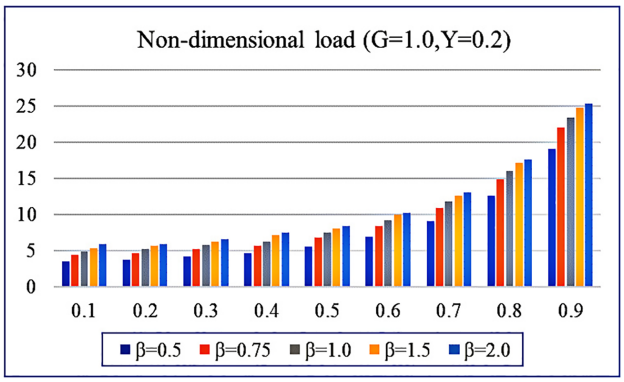

Figure 8: Load response to eccentricity for smooth and rough elliptic bore Case II.

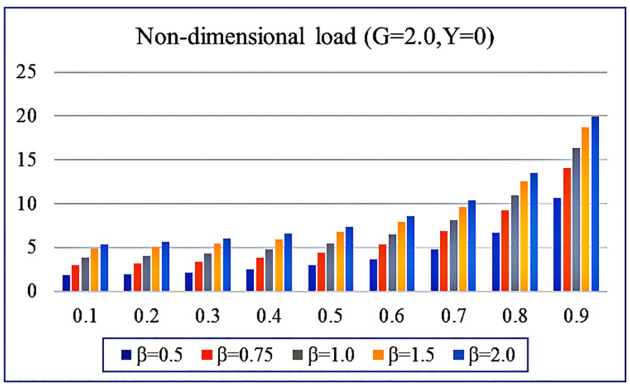

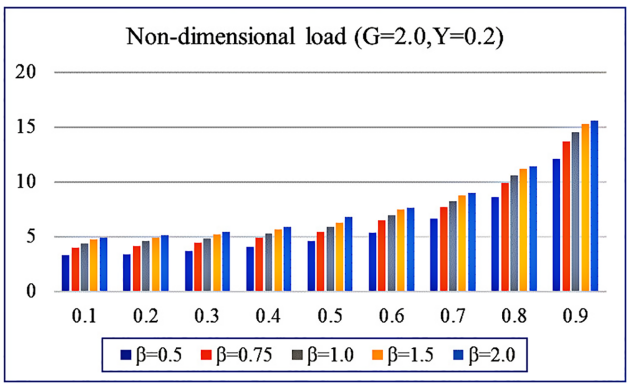

Figure 9: Load response to eccentricity for smooth and rough elliptic bore 3.

2017) used the proposed equations to determine the number of hidden nodes in the network. In the current analysis, we used the L–M back-propagation training algorithm to work with 5, 10, and 20 hidden nodes and observe the error convergence. The best convergence is found in the case of 20 nodes. As shown in Fig. 4, in the architecture diagram, the nodes are arranged in two layers, each containing ten hidden nodes.

Figure 5 shows the combined flow chart for numerical and ANN models. Here, the Reynolds equation is solved for the hydrodynamic pressure, and then load capacity, friction, and flow-in are estimated for the smooth and rough case. For the ANN model, four inputs and six outputs were set. The ANN model started with the input of data from the numerical model uploaded to MATLAB neural network tool in a matrix form. Now, the data are categorized as trained data set and test data set. It was followed by a network setting, network training, plotting, and network testing to receive data output. If the error in trained data and test data is not acceptable, then the network training was repeated. Once the error is permitted, the mapping of ANN output is carried out.

3. Results and Discussion

3.1. Analysis of numerical result

The numerical model developed here is validated with the work of Christensen and Tonder (1973). For the comparison, the model is converted to a one-dimensional circular case. Figure 6a–b shows the validation bar chart for short ($\beta = 0.5$) and finite ($\beta = 1.0$) journal bearing.

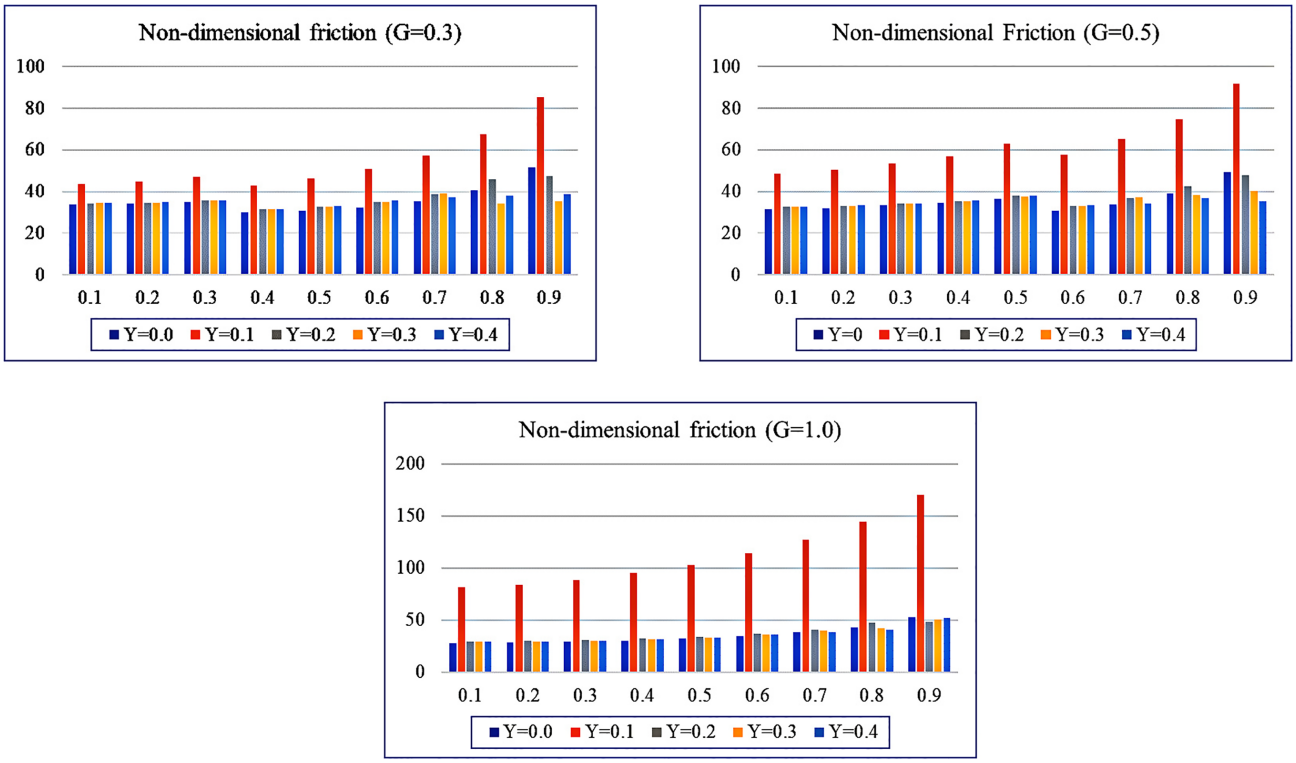

Figure 10: Friction response to eccentricity for smooth and rough elliptic bore.

At different eccentricities (0.1, 0.3, 0.5, 0.7, and 0.9), the LCC for the current case is compared with that of Christensen and Tonder (1973) for roughness parameters ($Y = 0.1$ and 0.2). The validation shows that the difference between this work and Christensen and Tonder (1973) is less than 5%. Hence, it is encouraging to adopt this model for further analysis of rough elliptic bore journal bearing.

Figure 7a–b shows the load response to eccentricities for short ($\beta = 0.5$ and 0.75), finite ($\beta = 1.0$), and long ($\beta = 1.5$ and 2.0) journal bearing at ($Y = 0.0$ and 0.2). For smooth case ($Y = 0.0$) at $G = 0.5$, the LCC increases 12 times between eccentricities of 0.1 and 0.9. At each eccentric position, the LCC increases in order of short, finite, and long journal bearing. The highest LCC at 0.9 eccentricity decreases by 20% due to the presence of roughness parameters ($Y = 0.2$).

Figure 8a–b shows the bar chart of the smooth and rough elliptic bore at $G = 1.0$. The highest value of LCC decreases by 25% due to roughness value of $Y = 0.2$. With the increase in eccentricity from 0.1 to 0.9, the LCC increases by six times for smooth bearing, while in the case of rough bearing, the increase observed is eight times for all short, long, and finite bearing cases.

Figure 9a–b shows the LCC bar chart of $G = 2.0$. In this case for smooth, the LCC changes four times between eccentricities of 0.1 and 0.9. While for rough case ($Y = 0.2$), it increases three times. Based on Figs 6–8, it was observed that by increasing non-circularity $0.5 < G < 2.0$, the maximum LCC reduces as $60 < W < 20$ in smooth bearing case. While for rough cases ($Y = 0.2$) for $0.5 < G < 2.0$, the LCC decreases as $40 < W < 15$.

Figure 10a–c shows the non-dimensional friction force at a different value of non-circularities. $G = 0.3$, 0.5, and 1.0 for different roughness parameters ($Y = 0$, 0.1, 0.2, 0.3, and 0.4). For all cases, the maximum friction occurs at $Y = 0.1$. The highest value of friction increases with an increase in non-circularity value. It is 84, 92, and 165 at $G = 0.3$, 0.5, and 1.0, respectively. For all non-circularity cases, the friction force increases two times between eccentricities of 0.1 and 0.9. From $Y = 0.0$ to 0.1, the friction increases suddenly, and later beyond 0.1 and 0.4, it decreases and becomes even less than the smooth case.

Table 5: Comparison of various bearing parameters (non-dimensional).

ε	W_c	W_{re}	F_c	F_{re}	Q_c	Q_{re}
0.1	3.093	4.9387	33.91	81.85	0.3784	2.179
0.2	3.6028	5.2531	33.99	83.75	0.3874	2.1867
0.3	4.5363	5.806	34.88	88.09	0.4506	2.0464
0.4	5.905	6.3253	29.88	95.06	0.5468	2.0671
0.5	8.0067	7.5557	30.7	102.48	0.6429	2.0958
0.6	10.9951	9.3407	32.34	114.5	0.684	2.132
0.7	15.58	11.9975	35.25	126.9	0.7682	2.1783
0.8	23.5057	16.443	40.51	144.67	0.8491	2.0404
0.9	41.4012	24.5413	51.43	170.48	0.9263	2.1035

(i) W_c: LCC (conventional bearing); W_{re}: LCC (rough elliptic bore bearing).
(ii) F_c: Friction (conventional bearing); F_{re}: Friction (rough elliptic bore bearing).
(iii) Q_c: Flow-in (conventional bearing); Q_{re}: Flow-in (rough elliptic bore bearing).

Figure 10a–c shows the non-dimensional flow-in for short, finite, and long journal bearing. As flow-in is in the circumferential direction, it is independent of whether the bearing is short, finite, or long. The flow-in increases with increase in non-circularity and is 8.5% more between $G = 0.5$ and 1.0. Table 5 shows the comparison of output parameters between the conventional bearing and rough elliptic bore bearing. The output parameters are more in rough elliptic case.

In the current program, the load, friction, and flow-in could be computed for different eccentricities, non-circularities,

Table 6: Neural network window display.

Algorithm			
Data division		Random (dividerand)	
Training		L–M	
Performance		MSE	
Calculations		MEX	
Progress	**Range**		**Current display**
Epoch	0–1000		Seven iterations
Time			0:00:00
Performance	2.49–0.00		1.57e-28
Gradient	45.1–1.00e-10		3.95e-13
Mu	0.00100–1.00e + 10		
Validation check	0–70		7
Plots			
Performance		Plot perform	
Training state		Plot train state	
Regression		Plot regression	

Table 7: First training observation table of simulated data I (experimental outputs).

Run	Factor-1 (ε)	Factor-2 (β)	Factor-3 (G)	Factor-4 (Y)	Experimental outputs					
					W_{is}	W_{th}	F_{is}	F_{th}	Q_{is}	Q_{th}
1	0.3	0.5	0.5	0.1	3.9176	1.302	52.95	22.51	4.4394	5.2438
2	0.3	0.5	0.5	0.2	3.882	1.302	33.85	14.83	4.4388	5.2429
3	0.3	0.5	0.5	0.3	3.8245	1.3026	33.73	14.83	4.4382	5.2415
4	0.3	1	1	0.1	5.806	3.432	88.09	46.01	4.8875	5.8628
5	0.3	1	1	0.2	5.7681	3.432	30.83	13.12	4.8875	5.8605
6	0.3	1	1	0.3	5.7063	3.432	30.12	13.12	4.8875	5.8567
7	0.3	2	2	0.1	5.4342	3.214	94.27	58.46	5.2134	6.342
8	0.3	2	2	0.2	5.41	3.321	38.32	15.43	5.1121	6.123
9	0.3	2	2	0.3	5.13	3.133	36.31	14.35	5.0032	6.0021
10	0.5	0.5	1	0.1	5.6321	1.7324	102.67	42.15	5.5016	7.0872
11	0.5	0.5	1	0.2	5.5731	1.7324	33.53	12.98	5.5016	7.0863
12	0.5	0.5	1	0.3	5.4786	1.7324	32.71	12.98	5.5016	7.0847
13	0.5	1	2	0.1	5.9403	2.1872	95.36	36.65	5.324	6.832
14	0.5	1	2	0.2	5.9018	2.3413	40.32	14.32	5.123	6.342
15	0.5	1	2	0.3	5.81	2.43	38.43	13.78	5.006	6.213
16	0.5	2	0.5	0.1	10.5943	5.397	63.31	54.38	5.5016	5.7148
17	0.5	2	0.5	0.2	10.465	5.3972	38.23	31.18	5.5016	5.7116
18	0.5	2	0.5	0.3	10.2577	5.3972	38.09	31.18	5.5016	5.7063
19	0.8	0.5	2	0.1	8.8186	4.345	68.231	40.824	5.756	5.821
20	0.8	0.5	2	0.2	8.6272	4.234	40.13	40.021	5.754	5.281
21	0.8	0.5	2	0.3	8.2216	4.132	40.012	38.293	5.345	5.221
22	0.8	1	0.5	0.1	24.5895	6.19	74.78	31.49	5.9745	6.0376
23	0.8	1	0.5	0.2	23.8265	6.19	42.39	17.11	5.9745	6.0356
24	0.8	1	0.5	0.3	22.7026	6.19	40.52	17.11	5.9745	6.0324
25	0.8	2	1	0.1	17.9991	6.3785	17.9991	6.3785	6.4226	6.2705
26	0.8	2	1	0.2	17.6003	6.3785	17.6003	6.3785	6.4226	6.2675
27	0.8	2	1	0.3	16.7014	6.3785	16.7014	6.3785	6.4226	6.2625

roughness, and *L*/*D* ratio. Such data are further used as input for the ANN model for data training and simulation.

3.2. ANN model architecture and training

A forward feedback propagation multilayer ANN is used for modelling, training, and testing using MATLAB. As the activation transfer functions, TANSIG (hyperbolic tangent sigmoid) function, and linear transfer function (purelin) were used. However, the back-propagation function that updates weight and bias values according to L–M optimization (trainlm) was used as an algorithm for training. Such algorithm was chosen due to its high accuracy in prediction and fast convergence. The hidden layers consist of 20 neurons, and the output layer consists of 6 neurons.

3.3. Process parameters for the ANN model

In this model, 27 data sets are used by varying the input parameters such as non-circularity (*G*), *l*/*d* ratios (β), roughness factors (Y), and eccentricities (ε). These data sets have the corresponding targets as both isothermal and thermal load (W_{is},

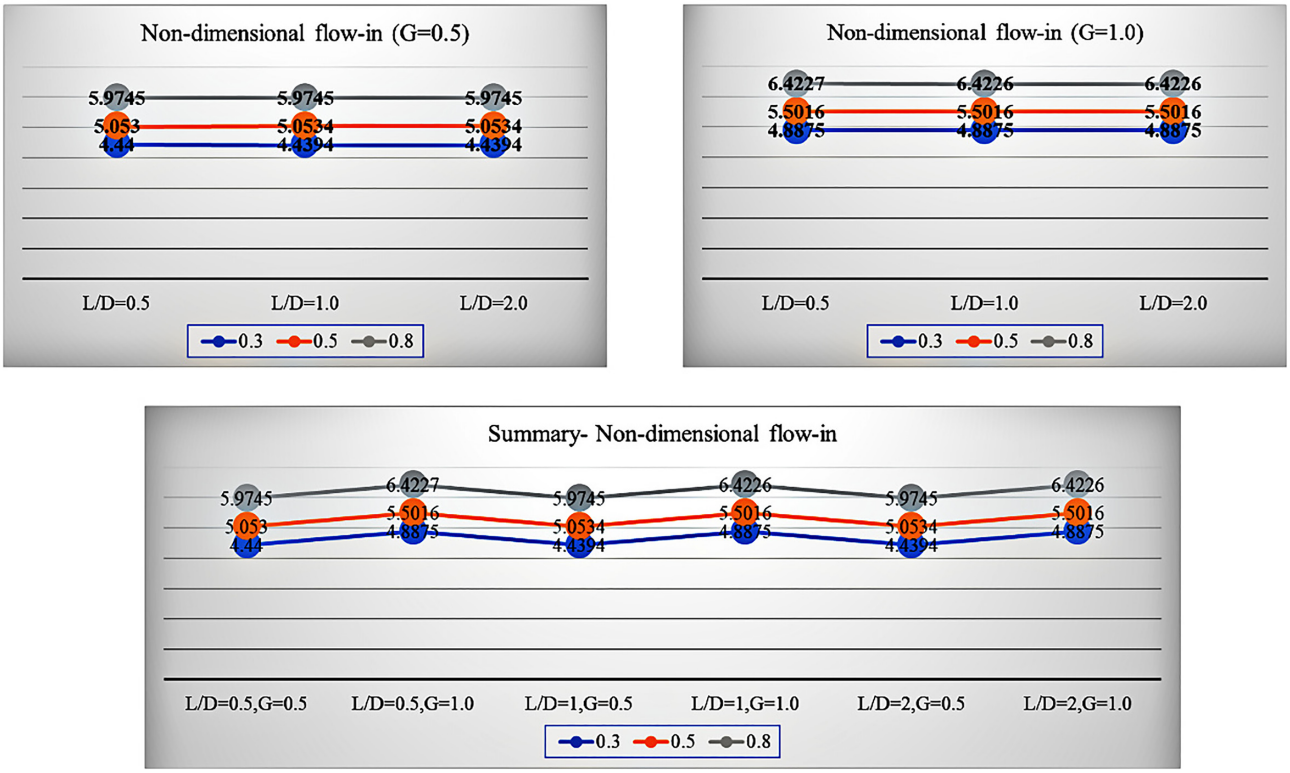

Figure 11: Flow-in response to variation of non-circularity, eccentricities, and roughness parameter.

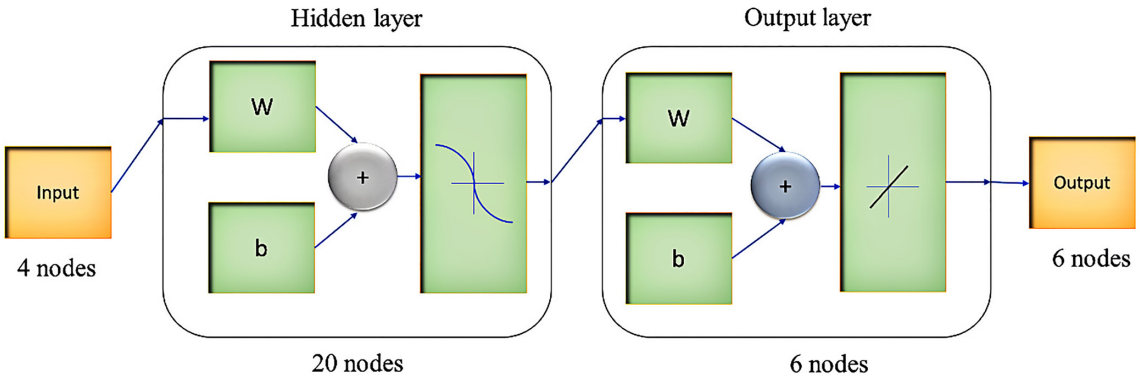

Figure 12: Network training window.

W_{th}), frictional forces (F_{is}, F_{th}), and flow into the bearing (Q_{is}, Q_{th}) as given in the tabular form. These data sets were processed for training, validation, and testing. The output parameters were predicted, and the performance was considered from the mean square error (MSE). According to the construction, it is a two-layer feed-forward network with tan sigmoid and linear output neurons. It can give an excellent fit to this complicated problem.

3.4. MSE of performance plot using ANN

As the MSE reaches its minimum value, the training was stopped. Table 7 shows the first training results and the errors of every data set. As per the performance graph, the minimum MSE of the model after several training cycles shows 0.68008 as the best validation. This structure is finally used for the ANN prediction system. Table 3 shows the comparison of experimental data and the predicted data for the input data sets. It is shown in Fig. 11 that with a minimal iteration (seven), the data are validated and attain an accuracy of 0.68008. Here, training and testing curves are entirely overlapping, which is a good indication that there is a minor error in the validation check.

The training curve in Fig. 13 shows the gradual decrease in MSE over the epochs, and in the seventh epoch, it becomes zero, indicating the early completion of the training based on similar value and pattern detection. The initial stages, however, were completing the training cycle in 70–90 epochs, which eventually reduced due to the repetition of results and pattern.

3.5. Regression plots of training, testing, validation using ANN

Tables 7–9 show the first training observations for experimental outputs, training data, and error in the primary analysis.

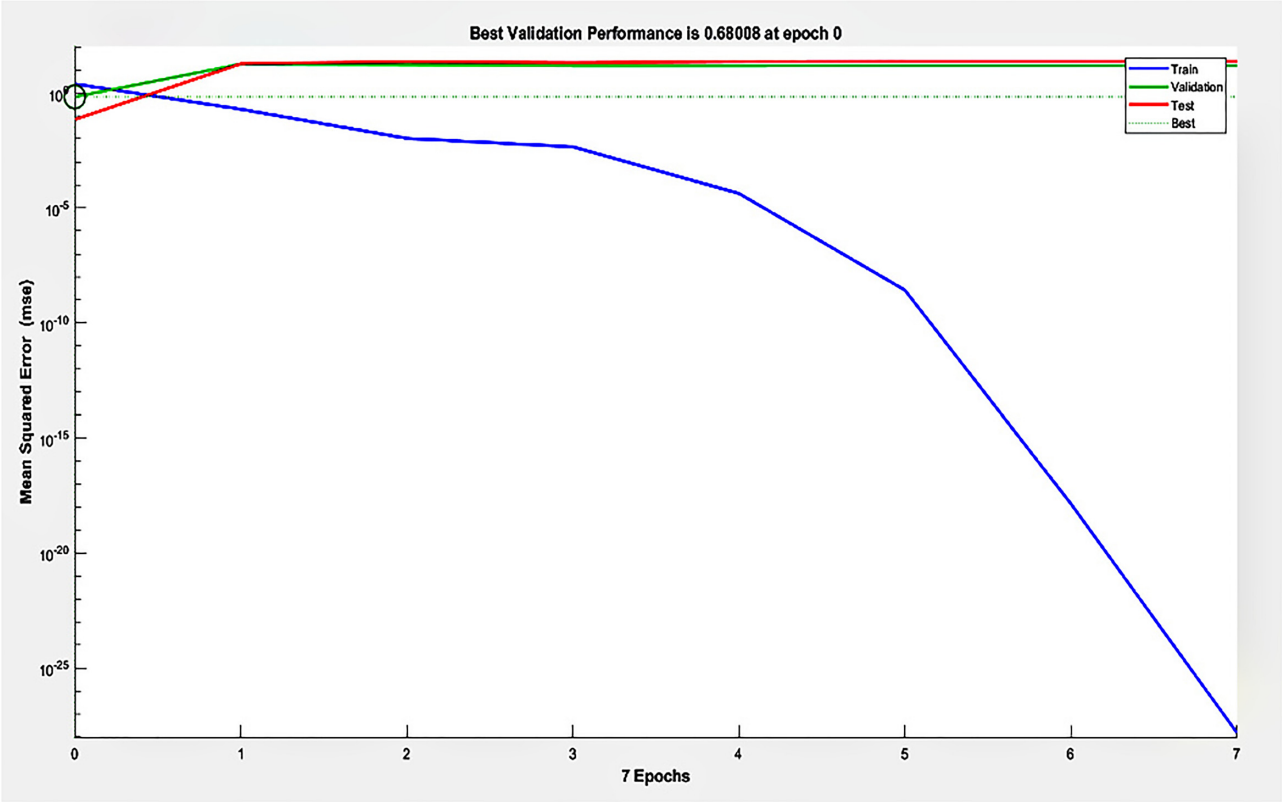

Figure 13: Validation of performance with mean square error.

Table 8: First training observation table of simulated data II (training data).

Run	Factor-1 (ε)	Factor-2 (β)	Factor-3 (G)	Factor-4 (Y)	Training data					
					W_{is}	W_{th}	F_{is}	F_{th}	Q_{is}	Q_{th}
1	0.3	0.5	0.5	0.1	3.962551	1.478617	53.07155	22.52402	4.551524	5.460392
2	0.3	0.5	0.5	0.2	3.883718	1.684947	32.70376	6.3785	4.996161	6.625786
3	0.3	0.5	0.5	0.3	4.201598	1.361866	32.37818	6.3785	5.847097	6.83724
4	0.3	1	1	0.1	5.804787	1.30645	88.11588	46.00925	4.843563	5.957066
5	0.3	1	1	0.2	5.76862	1.331829	30.82933	13.10492	4.859897	5.705345
6	0.3	1	1	0.3	5.697839	1.305551	30.12345	6.378501	4.911592	5.899324
7	0.3	2	2	0.1	3.824935	3.219166	94.26723	58.42768	5.233276	6.339558
8	0.3	2	2	0.2	3.825398	4.972288	39.43574	10.8877	4.638372	5.485973
9	0.3	2	2	0.3	3.868563	1.960157	34.25957	6.380608	4.865232	6.423138
10	0.5	0.5	1	0.1	5.635592	1.543351	102.5553	42.13741	5.439068	6.822277
11	0.5	0.5	1	0.2	4.540916	1.322737	32.04239	6.3785	5.468863	6.668719
12	0.5	0.5	1	0.3	5.481786	1.328806	32.70506	6.3785	5.528242	6.974799
13	0.5	1	2	0.1	5.936903	2.173041	95.37896	36.66705	5.313265	6.94684
14	0.5	1	2	0.2	5.906886	2.335576	40.31716	14.32401	5.046067	6.289983
15	0.5	1	2	0.3	5.80769	2.466069	38.42528	13.78715	5.078906	6.209455
16	0.5	2	0.5	0.1	10.59625	6.36486	63.3785	6.3785	5.510916	5.7629
17	0.5	2	0.5	0.2	10.45416	5.422999	38.27635	6.3785	5.548423	5.70291
18	0.5	2	0.5	0.3	9.770155	1.490455	34.3577	6.3785	6.356785	6.912747
19	0.8	0.5	2	0.1	8.830468	4.368222	68.19568	58.46	5.833418	5.83428
20	0.8	0.5	2	0.2	8.627354	4.210859	40.14663	40.02834	5.756091	5.406863
21	0.8	0.5	2	0.3	8.21909	4.140153	40.01349	38.291	5.31386	5.273918
22	0.8	1	0.5	0.1	24.53371	6.3705	74.76906	6.3785	5.990167	6.02237
23	0.8	1	0.5	0.2	23.82795	6.261925	42.39088	6.3785	5.973234	6.076912
24	0.8	1	0.5	0.3	18.07396	2.44515	37.86881	6.3785	6.015176	7.036599
25	0.8	2	1	0.1	17.99805	6.377965	17.99534	6.3785	6.296026	6.247124
26	0.8	2	1	0.2	19.69706	6.377685	16.70198	6.3785	6.122437	5.804993
27	0.8	2	1	0.3	16.7014	6.247057	16.70708	6.3785	6.29855	6.239001

Table 9: First training observation table of simulated data III (errors).

Run	Factor-1 (ε)	Factor-2 (β)	Factor-3 (G)	Factor-4 (Y)	Error					
					W_{is}	W_{th}	F_{is}	F_{th}	Q_{is}	Q_{th}
1	0.3	0.5	0.5	0.1	−0.04495	−0.17662	−0.12155	−0.01402	−0.11212	−0.21659
2	0.3	0.5	0.5	0.2	−0.00172	−0.38295	1.146241	8.4515	−0.55736	−1.38289
3	0.3	0.5	0.5	0.3	−0.3771	−0.0592	1.35182	8.4515	−1.4089	−1.59574
4	0.3	1	1	0.1	0.001213	2.12555	−0.02588	0.000746	0.043937	−0.09427
5	0.3	1	1	0.2	−0.00052	2.100171	0.000665	0.015082	0.0027603	0.155155
6	0.3	1	1	0.3	0.008461	2.126449	−0.00345	6.741499	−0.02049	0.04262
7	0.3	2	2	0.1	1.609265	−0.00517	0.002766	0.03232	−0.01988	0.002442
8	0.3	2	2	0.2	1.584602	−1.65129	−1.11574	4.542305	0.473728	0.637027
9	0.3	2	2	0.3	1.261437	1.172843	2.050428	7.969392	0.137968	−0.42104
10	0.5	0.5	1	0.1	−0.00349	0.189049	0.114737	0.012593	0.06532	0.264923
11	0.5	0.5	1	0.2	1.032184	0.409663	1.487613	6.6015	0.032737	0.417581
12	0.5	0.5	1	0.3	−0.0319	0.403594	0.004935	6.6015	−0.02664	0.109901
13	0.5	1	2	0.1	0.003397	0.014159	−0.01896	−0.01705	0.010735	−0.11484
14	0.5	1	2	0.2	−0.00509	0.005724	0.002873	−0.00401	0.076933	0.052017
15	0.5	1	2	0.3	0.00231	−0.03607	0.005417	−0.00715	−0.07291	0.003545
16	0.5	2	0.5	0.1	−0.00195	−0.96786	0.031298	48.0015	−0.00932	−0.0481
17	0.5	2	0.5	0.2	0.01084	−0.0258	−0.04635	24.8015	−0.85516	−1.220645
18	0.5	2	0.5	0.3	0.487545	3.906745	3.732297	24.8015	−0.85516	−1.20645
19	0.8	0.5	2	0.1	−0.01187	−0.02322	0.035325	−17.636	−0.07742	−0.01328
20	0.8	0.5	2	0.2	−0.00015	0.023141	−0.01663	−0.00734	−0.00209	−0.12586
21	0.8	0.5	2	0.3	0.00251	−0.00815	−0.00149	0.00203	0.03114	−0.05292
22	0.8	1	0.5	0.1	0.055789	−0.18075	0.010941	25.1115	−0.01567	0.01523
23	0.8	1	0.5	0.2	−0.00145	−0.07192	−0.00088	10.7315	0.001266	−0.04131
24	0.8	1	0.5	0.3	4.628642	3.74485	2.651186	10.7315	−0.13068	−1.0042
25	0.8	2	1	0.1	0.001049	0.000535	0.003761	−4.49E-9	0.126574	0.023376
26	0.8	2	1	0.2	−2.09676	0.000815	0.898323	0	0.300163	0.462507
27	0.8	2	1	0.3	3.41E-06	0.131443	−0.00586	0	0.12405	0.023499

Table 10: Final training observation table of trained simulated data I (experimental outputs).

Run	Factor-1 (ε)	Factor-2 (β)	Factor-3 (G)	Factor-4 (Y)	Experimental outputs					
					W_{is}	W_{th}	F_{is}	F_{th}	Q_{is}	Q_{th}
1	0.3	0.5	0.5	0.1	3.9176	1.302	52.95	22.51	4.4394	5.2438
2	0.3	0.5	0.5	0.2	3.882	1.302	33.85	14.83	4.4388	5.2429
3	0.3	0.5	0.5	0.3	3.8245	1.3026	33.73	14.83	4.4382	5.2415
4	0.3	1	1	0.1	5.806	3.432	88.09	46.01	4.8875	5.8628
5	0.3	1	1	0.2	5.7681	3.432	30.83	13.12	4.8875	5.8605
6	0.3	1	1	0.3	5.7063	3.432	30.12	13.12	4.8875	5.8567
7	0.3	2	2	0.1	5.4342	3.214	94.27	58.46	5.2134	6.342
8	0.3	2	2	0.2	5.41	3.321	38.32	15.43	5.1121	6.123
9	0.3	2	2	0.3	5.13	3.133	36.31	14.35	5.0032	6.0021
10	0.5	0.5	1	0.1	5.6321	1.7324	102.67	42.15	5.5016	7.0872
11	0.5	0.5	1	0.2	5.5731	1.7324	33.53	12.98	5.5016	7.0863
12	0.5	0.5	1	0.3	5.4786	1.7324	32.71	12.98	5.5016	7.0847
13	0.5	1	2	0.1	5.9403	2.1872	95.36	36.65	5.324	6.832
14	0.5	1	2	0.2	5.9018	2.3413	40.32	14.32	5.123	6.342
15	0.5	1	2	0.3	5.81	2.43	38.43	13.78	5.006	6.213
16	0.5	2	0.5	0.1	10.5943	5.397	63.31	54.38	5.5016	5.7148
17	0.5	2	0.5	0.2	10.465	5.3972	38.23	31.18	5.5016	5.7116
18	0.5	2	0.5	0.3	10.2577	5.3972	38.09	31.18	5.5016	5.7063
19	0.8	0.5	2	0.1	8.8186	4.345	68.231	40.824	5.756	5.821
20	0.8	0.5	2	0.2	8.6272	4.234	40.13	40.021	5.754	5.281
21	0.8	0.5	2	0.3	8.2216	4.132	40.012	38.293	5.345	5.221
22	0.8	1	0.5	0.1	24.5895	6.19	74.78	31.49	5.9745	6.0376
23	0.8	1	0.5	0.2	23.8265	6.19	42.39	17.11	5.9745	6.0356
24	0.8	1	0.5	0.3	22.7026	6.19	40.52	17.11	5.9745	6.0324
25	0.8	2	1	0.1	17.9991	6.3785	17.9991	6.3785	6.4226	6.2705
26	0.8	2	1	0.2	17.6003	6.3785	17.6003	6.3785	6.4226	6.2675
27	0.8	2	1	0.3	16.7014	6.3785	16.7014	6.3785	6.4226	6.2625

Similarly, Tables 10–12 show the final training observations for experimental outputs, training data, and error in the preliminary analysis.

From Fig. 14a–d, it is evident that the data fit well because of adequate training of the network. Finally, this neural network model is to predict directly the unknown parameters for the newer data sets in future. The regression coefficient or the coefficient of determination or the R-value gives outputs against the corresponding target values. When R is nearer to 1, the closer is the relation between the experimental and predicted data. It

Table 11: Final training observation table of trained simulated data II (training data).

Run	Factor-1 (ε)	Factor-2 (β)	Factor-3 (G)	Factor-4 (Y)	Training data					
					W_{is}	W_{th}	F_{is}	F_{th}	Q_{is}	Q_{th}
1	0.3	0.5	0.5	0.1	3.962551	1.478617	53.07155	22.52402	4.551524	5.460392
2	0.3	0.5	0.5	0.2	3.883718	1.684947	32.70376	6.3785	4.996161	6.625786
3	0.3	0.5	0.5	0.3	4.201598	1.361866	32.37818	6.3785	5.847097	6.83724
4	0.3	1	1	0.1	5.804787	1.30645	88.11588	46.00925	4.843563	5.957066
5	0.3	1	1	0.2	5.76862	1.331829	30.82933	13.10492	4.859897	5.705345
6	0.3	1	1	0.3	5.697839	1.305551	30.12345	6.378501	4.911592	5.899324
7	0.3	2	2	0.1	3.824935	3.219166	94.26723	58.42768	5.233276	6.339558
8	0.3	2	2	0.2	3.825398	4.972288	39.43574	10.8877	4.638372	5.485973
9	0.3	2	2	0.3	3.868563	1.960157	34.25957	6.380608	4.865232	6.423138
10	0.5	0.5	1	0.1	5.635592	1.543351	102.5553	42.13741	5.439068	6.822277
11	0.5	0.5	1	0.2	4.540916	1.322737	32.04239	6.3785	5.468863	6.668719
12	0.5	0.5	1	0.3	5.481786	1.328806	32.70506	6.3785	5.528242	6.974799
13	0.5	1	2	0.1	5.936903	2.173041	95.37896	36.66705	5.313265	6.94684
14	0.5	1	2	0.2	5.906886	2.335576	40.31716	14.32401	5.046067	6.289983
15	0.5	1	2	0.3	5.80769	2.466069	38.42458	13.78715	5.078906	6.209455
16	0.5	2	0.5	0.1	10.59625	6.36486	63.2787	6.3785	5.510916	5.7629
17	0.5	2	0.5	0.2	10.45416	5.422999	38.27635	6.3785	5.548423	5.70291
18	0.5	2	0.5	0.3	9.770155	1.490455	34.3577	6.3785	6.356758	6.912747
19	0.8	0.5	2	0.1	8.830468	4.368222	68.19568	58.46	5.833418	5.83428
20	0.8	0.5	2	0.2	8.627354	4.210859	40.14663	40.02834	5.756091	5.406863
21	0.8	0.5	2	0.3	8.21909	4.140153	40.01349	38.291	5.31386	5.273918
22	0.8	1	0.5	0.1	24.53371	6.37075	74.76906	6.3785	5.990167	6.02237
23	0.8	1	0.5	0.2	23.82795	6.261925	42.39088	6.3785	5.973234	6.076912
24	0.8	1	0.5	0.3	18.07396	2.44515	37.86881	6.3785	6.105176	7.036599
25	0.8	2	1	0.1	17.99805	6.377965	17.99534	6.3785	6.296026	6.247124
26	0.8	2	1	0.2	19.69706	6.377685	16.70198	6.3785	6.122437	5.804993
27	0.8	2	1	0.3	16.7014	6.247057	16.70708	6.3785	6.29855	6.239001

Table 12: Final training observation table of trained simulated data III (errors).

Run	Factor-1 (ε)	Factor-2 (β)	Factor-3 (G)	Factor-4 (Y)	Error					
					W_{is}	W_{th}	F_{is}	F_{th}	Q_{is}	Q_{th}
1	0.3	0.5	0.5	0.1	−0.04495	−0.17662	−0.12155	−0.01402	−0.11212	−0.21659
2	0.3	0.5	0.5	0.2	−0.00172	−0.38295	1.146241	8.4515	−0.55736	−1.38289
3	0.3	0.5	0.5	0.3	−0.3771	−0.05927	1.35182	8.4515	−1.4089	−1.59574
4	0.3	1	1	0.1	0.001213	2.12555	−0.02588	0.000746	0.043937	−0.09427
5	0.3	1	1	0.2	−0.00052	2.100171	0.000665	0.015082	0.027603	0.155155
6	0.3	1	1	0.3	0.008461	2.126449	−0.00345	6.741499	−0.02409	−0.04262
7	0.3	2	2	0.1	1.609265	−0.00517	0.002766	0.03232	−0.01988	0.002442
8	0.3	2	2	0.2	1.584602	−1.65129	−1.11574	4.542305	0.473728	0.637027
9	0.3	2	2	0.3	1.261437	1.172843	2.050428	7.969392	0.137968	−0.42104
10	0.5	0.5	1	0.1	−0.00349	0.189049	0.114737	0.012593	0.062532	0.264923
11	0.5	0.5	1	0.2	1.032184	0.409663	1.487613	6.6015	0.032737	0.417581
12	0.5	0.5	1	0.3	−0.00319	0.403594	0.004935	6.6015	−0.02664	0.109901
13	0.5	1	2	0.1	0.003397	0.014159	−0.01896	−0.01705	0.010735	−0.11484
14	0.5	1	2	0.2	−0.00509	0.005724	0.002837	−0.00401	0.076933	0.052017
15	0.5	1	2	0.3	0.00231	−0.03607	0.005417	−0.00715	−0.07291	0.003545
16	0.5	2	0.5	0.1	−0.00195	−0.96786	0.031298	48.0015	−0.00932	−0.0481
17	0.5	2	0.5	0.2	0.01084	−0.0258	−0.04635	24.8015	−0.04682	0.00869
18	0.5	2	0.5	0.3	0.487545	3.906745	3.732297	24.8015	−0.85516	−1.20645
19	0.8	0.5	2	0.1	−0.01187	−0.02322	0.035325	−17.636	−0.07742	−0.01328
20	0.8	0.5	2	0.2	−0.00015	0.023141	−0.01663	−0.00734	−0.00209	−0.12586
21	0.8	0.5	2	0.3	0.00251	−0.00815	−0.00149	0.002003	0.03114	−0.05292
22	0.8	1	0.5	0.1	0.055789	−0.18075	0.010941	25.1115	−0.01567	0.01523
23	0.8	1	0.5	0.2	−0.00145	−0.07192	−0.00088	10.7315	0.001266	−0.04131
24	0.8	1	0.5	0.3	4.628642	3.74485	2.651186	10.7315	−0.13068	−1.0042
25	0.8	2	1	0.1	0.001049	0.000535	0.003761	−4.49E-09	0.126574	0.023376
26	0.8	2	1	0.2	−2.09676	0.000815	0.898323	0	0.300163	0.462507
27	0.8	2	1	0.3	3.41E-06	0.131443	−0.00568	0	0.12405	0.023499

generally shows the quality of the network and how good it is capable of predicting data.

Figure 14 illustrates the training, validation, testing, and comprehensive set of *R*-values. It can be seen that *R*-value for the combined data set is 0.99757, which concludes that this network training is good, and can be used for quality data prediction. The training data give $R = 0.99654$, whereas validation data and testing data give *R*-values as 0.99931 and 0.99995, respectively. There are some residual data with unusual errors, which can be due to fewer data sets or the arbitrary behaviour of data

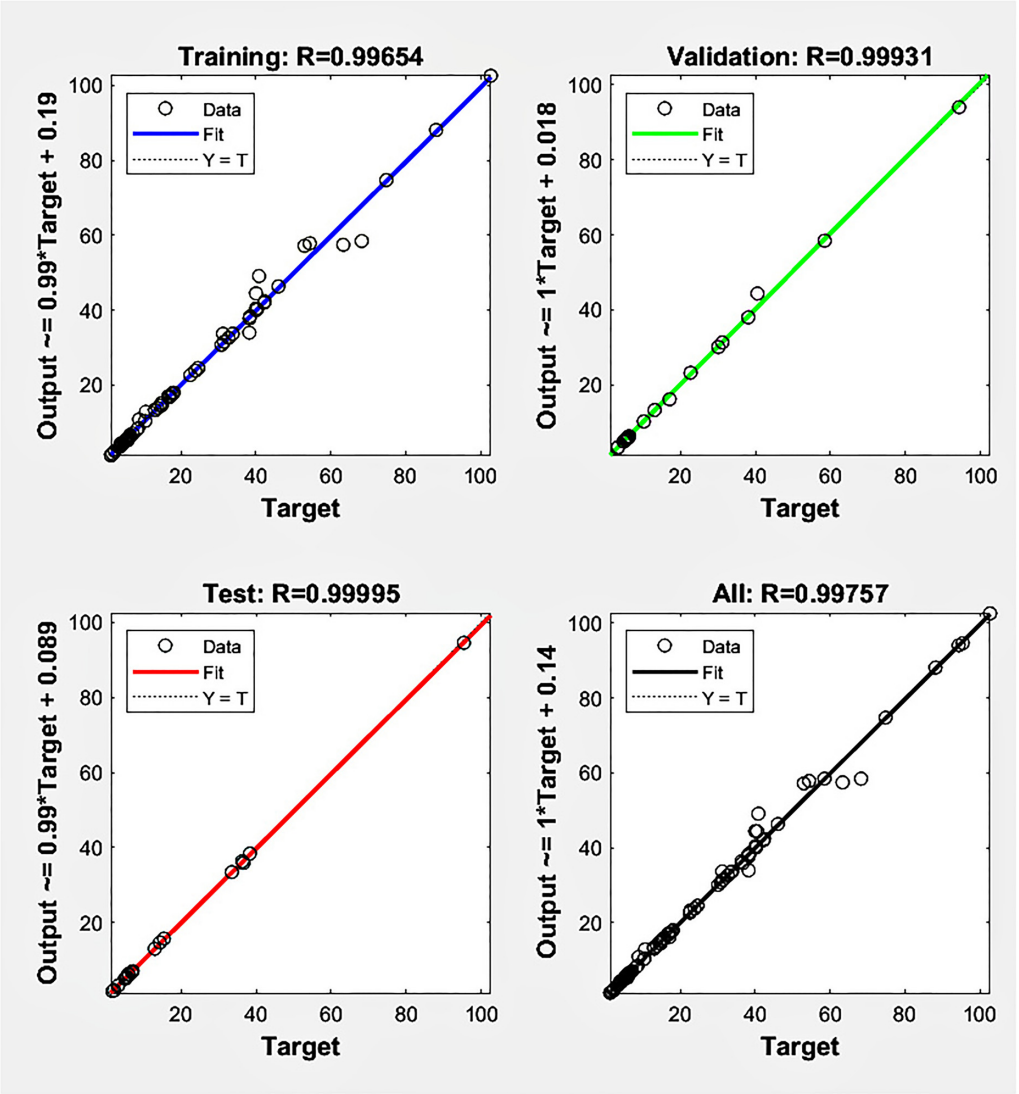

Figure 14: Regression plots for training and testing using MATLAB.

patterns around the parameters, or the errors in the experimental results. This can be improved by providing further training with more extensive data size by which the network performance will be enhanced.

3.6. Prediction of new data using ANN

The prediction of new data was conducted to validate the developed ANN model by using two sets of data by varying input parameters, i.e. non-circularity (G), L/D ratios (β), roughness factors (Y), and eccentricities (ε). Their corresponding outputs, i.e. isothermal and thermal load carrying capacities (W_{is}, W_{th}), frictional forces (F_{is}, F_{th}), and flow into the bearing (Q_{is}, Q_{th}), were obtained by simulating the prepared ANN model. The results obtained are given in Table 13.

It is observed that for an eccentricity of 0.4, an L/D ratio of 0.5 with a non-circularity factor of 2, and a roughness value of 0.1, isothermal (W_{is}) and thermal (W_{th}) LCCs are 8.32 and 1.32, respectively. The frictional forces (F_{is}) and (F_{th}) are 96.03 and 25.85, respectively. Also, the flow-ins to the bearing are (Q_{is}) 8.32 and (Q_{th}) 6.57, respectively. Similarly, the values for the second set also obtained corresponding outputs as shown in Table 13. Prediction is confirmed by comparing the new data and the previous range of values. Therefore, by considering the confidence level of 99.75% or the R-value of 0.99757, the predicted results are satisfactory.

4. Conclusion

The ANN prediction of the output parameters for the finite journal bearing is carried out and compared with the training results. The ANN model was developed based on the data obtained from the simulation results of rough elliptic bore journal bearing. It was trained and tested. The output process parameters, LCCs, frictional forces, and flow into the bearing were analysed and validated in this study and the results predicted are summarized as follows:

1. The LCC of journal bearing decreases with the increase in non-circularity, but the non-circularity value up to 1 is conducive for bearing operation as it gives better stability.

Table 13: Simulation results.

Sl. no.	Input parameters				Simulated data					
	Factor-1 (ε)	Factor-2 (β)	Factor-3 (G)	Factor-4 (Y)	W_{is}	W_{th}	F_{is}	F_{th}	Q_{is}	Q_{th}
1	0.4	0.5	2	0.1	8.323433	1.322677	96.03969	25.85195	4.05391	6.570336
2	0.6	0.5	1	0.2	5.762695	1.468324	45.51122	7.315798	5.884018	7.125625

2. Friction force increases with the increase in non-circularity, while the flow is independent of whether the bearing is short, finite, or long.
3. The ANN simulation predicts the combination of eccentricity, *L*/*D* ratio, non-circularity, and roughness parameters as (0.4, 0.5, 2, and 0.1) and (0.6, 0.5, 1, and 0.2), respectively, for best output with a confidence level of 99.75% or the *R*-value of 0.99757.

The limitation of this model is that it is very simple and deals with only a few eccentric positions of the shaft. It uses only 162 data points. The eccentricity range (0.1–0.9) could avail more data points for better bearing condition monitoring. Even the hybrid models, if developed, would predict more accurate results. The immediate application of this model is to bearing manufacturing industries, engaged in journal bearing manufacturing for automotive, aerospace, and heavy-duty machineries. Future work of this research is to develop a combined PSO-, ANN-, and ICA-based hybrid model for journal bearing design considering bore ellipticity and non-circularity.

Conflict of interest statement

None declared.

References

Armaghani, D. J., Hasanipanah, M., & Tonnizam Mohamad, E. (2015). A combination of the ICA-ANN model to predict air-overpressure resulting from blasting. *Engineering with Computers*, *32*(1), 155–171. https://doi:10.1007/s00366-015-0408-z.

Armaghani, D. J., Shoib, R. S. N. S. B. R., Faizi, K., & Rashid, A. S. A. (2015). Developing a hybrid PSO–ANN model for estimating the ultimate bearing capacity of rock-socketed piles. *Neural Computing and Applications*, *28*(2), 391–405. https://doi:10.1007/s00521-015-2072-z.

Armaghani, D. J., Hasanipanah, M., Mahdiyar, A., Abd Majid, M. Z., Bakhshandeh Amnieh, H., & Tahir, M. M. D. (2016). Airblast prediction through a hybrid genetic algorithm-ANN model. *Neural Computing and Applications*, *29*(9), 619–629. https://doi:10.1007/s00521-016-2598-8.

Armaghani, D. J., Mohamad, E. T., Narayanasamy, M. S., Narita, N., & Yagiz, S. (2017). Development of hybrid intelligent models for predicting TBM penetration rate in hard rock condition. *Tunnelling and Underground Space Technology*, *63*, 29–43. https://doi:10.1016/j.tust.2016.12.009.

Bhowmik, K. L., Debnath, A., Nath, R. K., & Saha, B. (2017). Synthesis of MnFe2O4 and Mn3O4 magnetic nano-composites with enhanced properties for adsorption of Cr (VI): Artificial neural network modelling. *Water Science and Technology*, *76*(12), 3368–3378. https://doi:10.2166/wst.2017.501.

Bhowmik, M., Debnath, A., & Saha, B. (2019). Fabrication of mixed phase CaFe2O4 and MnFe2O4 magnetic nanocomposite for enhanced and rapid adsorption of methyl orange dye: Statistical modelling by neural network and response surface methodology. *Journal of Dispersion Science and Technology*, *41*(13), 1–12. https://doi:10.1080/01932691.2019.1642209.

Binu, K. G., Shenoy, B. S., Rao, D. S., & Pai, R. (2014). A variable viscosity approach for the evaluation of load carrying capacity of oil lubricated journal bearing with TiO2 nanoparticles as lubricant additives. *Procedia Material Science*, *6*, 1051–1067. https://doi.org/10.1016/j.mspro.2014.07.176.

Christensen, H. (1969). Stochastic models for hydrodynamic lubrication of rough surfaces. *Proceedings of the Institution of Mechanical Engineers*, *184*(Part-I), 1013–1025. https://doi.org/10.1243%2FPIME_PROC_1969_184_074_02.

Christensen, H., & Tonder, K. (1973). The hydrodynamic lubrication of rough journal bearings. *Journal of Lubrication Technology, Transactions of the ASME*, *72*, 166–172. https://doi.org/10.1115/1.3451759.

Crosby, W. A. (1992). An investigation of performance of journal bearings with slightly irregular bore. *Tribology International*, *25*(3), 199–204. https://doi.org/10.1016/0301-679X(92)90049-S.

Deb, A., Kanmani, M., Debnath, A., Bhowmik, K. L., & Saha, B. (2017). Preparation and characterization of magnetic CaFe2O4 nanoparticles for efficient adsorption of toxic Congo Red dye from aqueous solution: Predictive modelling by artificial neural network. *Desalination and Water Treatment*, *57*(29), 13549–13560. https://doi:10.1080/19443994.2015.1060540.

Debnath, A., Deb, K., Chattopadhyay, K. K., & Saha, B. (2015). Methyl orange adsorption onto simple chemical route synthesized crystalline α-Fe2O3nanoparticles: Kinetic, equilibrium isotherm, and neural network modelling. *Desalination and Water Treatment*, *57*(29), 13549–13560. https://doi:10.1080/19443994.2015.1060540.

Debnath, A., Deb, K., Das, N. S., Chattopadhyay, K. K., & Saha, B. (2015). Simple chemical route synthesis of Fe2O3Nanoparticles and its application for adsorptive removal of congo red from aqueous media: Artificial neural network modelling. *Journal of Dispersion Science and Technology*, *37*(6), 775–785. https://doi:10.1080/01932691.2015.1062772.

Genel, K., Kurnaz, S. C., & Durman, M. (2003). Modeling of tribological properties of alumina fiber reinforced zinc–aluminum composites using artificial neural network. *Materials Science and Engineering A*, *363*, 203–210. https://dx.doi.org/10.1016/S0921-5093(03)00623-3.

Hayajneh, M., Hassan, A. M., Alrashdan, A., & Mayyas, A. T. (2009). Prediction of tribological behavior of aluminum–copper based composite using artificial neural network. *Journal of Alloys and Compounds*, *470*, 584–588. https://dx.doi.org/10.1016/j.jallcom.2008.03.035.

Kannaiyan, M., Govindan, K., & Thankachi Raghuvaran, J. G. (2019). Prediction of specific wear rate for LM25/ZrO2 composites using Levenberg–Marquardt backpropagation algorithm. *Journal of Materials Research and Technology*, *9*(1), 530–538. https://doi:10.1016/j.jmrt.2019.10.082.

Laad, M., & Jatti, V. K. S. (2018). Titanium oxide nanoparticles as additives in engine oil. *Journal of King Saud University*

- *Engineering Sciences*, *30*(2), 116–122. https://doi:10.1016/j.jksues.2016.01.008.

Leema, N., Radha, P., Vettivel, S. C., & Nehemiah, K. (2015). Characterization, pore size measurement and wear model of an intered Cu–W nano composite using radial basis functional neural network. *Materials and Design*, *68*, 195–206. https://dx.doi.org/10.1016/j.matdes.2014.11.035.

Li, C., Du, J., Zhu, J., & Yao, Y. (2019). Effects of structural parameters on the load carrying capacity of the multi-leaf gas foil journal bearing based on contact mechanics. *Tribology International*, *131*, 318–331. https://doi.org/10.1016/j.triboint.2018.09.003.

Liang, P., Lu, C., Pan, W., & Li, S. (2014). A new method for calculating the static performance of hydrostatic journal bearing. *Tribology International*, *77*, 72–77. https://doi.org/10.1016/j.triboint.2014.04.019.

Mishra, P. C. (2013). Mathematical modeling of stability in rough elliptic bore misaligned journal bearing considering thermal and non-Newtonian effects. *Applied Mathematical Modelling*, *37*, 5896–5912. https://doi.org/10.1016/j.apm.2012.11.020.

Pai, R., Rao, D. S., Shenoy, B. S., & Pai, R. S. (2012). Stability characteristics of a Tri-taper journal bearing: A linearized perturbation approach. *Journal of Materials Research and Technology*, *1*(2), 84–90. https://doi:10.1016/s2238-7854(12)70016-9.

Parrales, A., Hernández-Pérez, J., Flores, O., Hernandez, H., Gómez-Aguilar, J., Escobar-Jiménez, R., & Huicochea, A. (2019). Heat transfer coefficients analysis in a helical Double-Pipe evaporator: Nusselt number correlations through artificial neural networks. *Entropy*, *21*(7), 689. https://doi:10.3390/e21070689.

Rashed, F. S., & Mahmoud, T. S. (2009). Prediction of wear behaviour of A356/SiCp MMCs using neuralnetworks. *Tribology International*, *42*, 642–648. https://dx.doi.org/10.1016/j.triboint.2008.08.010.

Shahnazar, S., Bagheri, S., & Abd Hamid, S. B. (2016). Enhancing lubricant properties by nanoparticle additives. *International Journal of Hydrogen Energy*, *41*(4), 3153–3170. https://doi:10.1016/j.ijhydene.2015.12.040.

Sharma, A., Sharma, H., Sahoo, P. K., Tripathi, R. K., & Meher, L. C. (2015). ANN based modeling of performance and emission characteristics of diesel engine fuelled with polanga biodiesel at different injection pressures. *International Energy Journal*, *15*, 57–72. https://dx.doi.org/10.1080/01430750.2015.1023466.

Shen, X., Liu, Y., Cao, L., & Chen, X. (2012). Numerical Simulation of sliding wear for Self-lubricating spherical plain bearings. *Journal of Materials Research and Technology*, *1*(1), 8–12. https://doi:10.1016/s2238-7854(12)70003-0.

Sivák, M., Šipoš, Ľ., & Sivák, B. (1981). Load-carrying capacity of a journal bearing under dynamic loading. *Wear*, *66*(3), 345–354. https://doi.org/10.1016/0043-1648(81)90127-7.

Xiao, G., & Zhu, Z. (2010). Friction materials development by using DOE/RSM and artificial neural network. *Tribology International*, *43*, 218–227. https://dx.doi.org/10.1016/j.triboint.2009.05.019.

Zhang, Z., Friedrich, K., & Velten, K. (2002). Prediction on tribological properties of short fibre composites using artificial neural networks. *Wear*, *252*, 668–675. https://dx.doi.org/10.1016/S0043-1648(02)00023-6.